



Multi-channel fusion scale transformed signals with magnetic leakage for damage detection in steel wire ropes

Yazheng Wang^a, Peng Chen^{a,b}, Qingsheng Wei^a, Junyu Qi^c, Changbo He^d and Chengning Zhou^e

^aCollege of Engineering, Shantou University, Shantou, Guangdong, China; ^bKey Laboratory of Intelligent Manufacturing Technology, Ministry of Education, Shantou, Guangdong, China; ^cElectronics & Drives, Reutlingen University, Reutlingen, Germany; ^dCollege of Electrical Engineering and Automation, Anhui University, Hefei, China; ^eNuclear Power Institute of China, Chengdu, China

ABSTRACT

The timely identification and diagnosis of defects in Steel Wire Rope (SWR) is increasingly critical for ensuring structural integrity, operational safety, and maintenance efficiency across diverse industrial applications, including elevators, mining equipment, bridges, and cable-supported structures where unexpected failures could lead to catastrophic consequences. Current methodologies face significant challenges in detecting low-amplitude faults due to lift-off effects and complex noise environments, while existing localization frameworks struggle to balance detection accuracy with false omission rates. This research proposes a novel Multi-channel Fusion Scale Transformation (MCFST) approach utilizing magnetic flux leakage signals to address the challenges in detecting and localizing Local Faults (LFs), particularly those with diminished amplitude due to inherent weakness or lift-off effects amid comparable ambient noise. The proposed MFST develops a three-fold framework: a morphological-based signal enhancement technique that amplifies LF signals while preserving their essential characteristics, a Channel Shuffle and Fusion paradigm for ambient noise mitigation, and a computationally efficient localization framework combining template matching algorithms with LF-specific luminance characteristics. Experimental results demonstrate superior performance in detecting and precisely localizing LFs under challenging conditions, offering substantial improvements over existing approaches in both detection accuracy and computational efficiency...

ARTICLE HISTORY

Received 2 April 2025 Accepted 25 July 2025

KEYWORDS

Steel wire rope; nondestructive testing; local fault detection; magnetic flux leakage; condition monitoring

1. Introduction

Steel Wire Rope (SWR) has established itself as an indispensable structural component across a wide spectrum of industrial applications, including but not limited to elevators, cranes, bridges, and mining operations, primarily owing to its exceptional combination of mechanical properties such as high tensile strength, operational flexibility, and long-term durability. Nevertheless, during routine service conditions, these wire ropes are consistently subjected to numerous deteriorating factors, including sustained cyclic loading, environmental corrosion, and mechanical wear, which collectively contribute

to the initiation and propagation of Local Flaws (LFs) within the rope structure [1]. When such structural imperfections remain undetected and continue to develop, they can ultimately precipitate catastrophic failure events, thereby not only jeopardising operational safety but also potentially incurring substantial economic losses through equipment damage and operational downtime [2]. Consequently, the implementation of systematic inspection protocols and the development of advanced detection methodologies for SWR defects have become increasingly critical in maintaining the operational integrity and safety standards of modern industrial systems.

The evolution of non-destructive testing (NDT) for wire ropes represents a critical progression in structural health monitoring, beginning with rudimentary manual visual inspection [3-5] and subsequently evolving to incorporate more sophisticated methodologies such as acoustic signal analysis [4,6–11] and machine vision techniques [5,12– 14], primarily due to their non-invasive characteristics and superior accuracy potential. Within the acoustic emission domain, a significant breakthrough emerged when Schaal et al. [15] introduced an innovative damage detection algorithm founded on the Hilbert transform of guided ultrasonic waves, which consequently enables automated time-offlight analysis for precise defect localisation in multi-wire cables through distinctive wave packet identification. Furthermore, their comprehensive study not only assessed second harmonic waves but also conducted extensive amplitude comparisons against a hybrid finite-boundary element model, with their findings subsequently validated through rigorous laboratory experiments on both single and multi-wire systems. Complementing this research, Raišutis et al. [16] developed a sophisticated ultrasonicguided wave (UGW) method that seamlessly integrates semi-analytical finite element (SAFE) modelling with 3D FE analysis to thoroughly investigate wave propagation modes, dispersion curves, and excitation regions in multi-wire steel ropes with polymer cores. Although their experimental validation demonstrated remarkable capability in identifying specific defective strands within the rope's interior - a crucial aspect for assessing structural integrity under operational conditions - it is important to note that acoustic-based methods generally remain susceptible to environmental noise interference and frequently necessitate complex signal processing algorithms to reliably differentiate damage-related signals from background interference.

Furthermore, significant advancements in machine vision technology have substantially enhanced defect detection capabilities in industrial applications. Zhang et al. [17] pioneered a sophisticated machine-vision methodology that incorporates a segmentation template specifically designed to accommodate the intricate structural characteristics of steel wire ropes. This innovative approach successfully segments individual strands even under severely challenging industrial conditions, including the presence of lubricants, oil contamination, and variable illumination environments. Moreover, their research introduced a comprehensive defect detection framework that strategically utilises spatiotemporal grey sample sets for dynamic background modelling, consequently achieving remarkable accuracy and environmental adaptability for fracture detection in complex industrial settings. Building upon these developments, Huang et al. [18] systematically integrated surface image analysis with automated visual inspection – enhanced by a convolution neural network framework – to mitigate the subjectivity inherent in manual feature extraction. Their computer vision system not only demonstrated superior accuracy metrics but also achieved substantial improvements in processing efficiency

compared to conventional methodologies, thus establishing the considerable potential of automated visual technologies in industrial non-destructive testing applications. Nevertheless, it is crucial to acknowledge that vision-based methodologies remain fundamentally constrained by line-of-sight limitations and may exhibit reduced effectiveness in identifying internal or subsurface structural damage.

Given these inherent limitations in both acoustic and vision-based inspection techniques, particularly in challenging environmental conditions and internal defect detection scenarios, there has been a significant shift towards the adoption of magnetic flux leakage (MFL) testing [19-21], which offers distinct advantages in comprehensively detecting both surface and subsurface defects. However, the efficient processing and systematic analysis of the substantial data volumes generated by MFL systems has emerged as a significant technical challenge-one that machine learning approaches are particularly well-positioned to address [7,22-24]. In this domain, Kim et al. [25] successfully developed an integrated approach that combined MFL signal analysis with convolution neural networks (CNNs) to achieve accurate defect recognition, drawing on the well-established effectiveness of CNNs in feature extraction and classification by utilising both time and frequency domain analyses. Subsequently, Yi et al. [26] made substantial contributions to the field by advancing the integration of spectral-normalised neural Gaussian processes with GoogLeNet to enhance defect detection in steel wire ropes; their method incorporated uncertainty quantification via spectral normalisation and Gaussian process layers to cater to safety-critical applications. This sophisticated approach transformed 1D magnetic flux leakage signals into 2D Gramian angular field images, delivering state-ofthe-art performance in defect classification and out-of-distribution detection, as confirmed by careful ablation studies. Furthermore, Liu and Chen [27] employed a machine learning strategy that coupled MFL signal analysis with 1D CNNs - alongside Haar wavelet denoising and feature normalisation - to reach a testing accuracy of 98%, outperforming six traditional machine learning models in quantitative defect recognition while also highlighting limitations and suggesting future research directions. Liu et al. [28] introduced a hybrid conditional kernel SVM model, which achieved 91.7% classification accuracy and the shortest runtime among 12 machine learning models for wire rope defect recognition. Building upon these advances, Zhang et al. [29] proposed a quantitative identification method for detecting internal and external broken wires in steel wire ropes using continuous wavelet transform (CWT) and CNN, which automates fault information extraction from time-frequency images of magnetic flux leakage signals. The method eliminates complex signal processing and significantly improves detection accuracy and recognition performance compared to traditional methods. Similarly, Liu et al. [30] developed an MFL wire rope defect detection method that integrates an improved Hilbert transform with a long short-term memory (LSTM) neural network, achieving higher classification accuracy and faster runtime for multiple defect types under varied conditions.

Despite these significant technological advancements, machine learning methodologies continue to be constrained by the availability and quality of training datasets. Consequently, the transformation of signals obtained from MFL into images for subsequent analysis through digital image processing techniques [31,32] has progressively emerged as a predominant strategy for enhancing detection accuracy and operational flexibility. In this context, Zheng and Zhang [33]

developed an innovative unsaturated magnetic excitation-based MFL device for wire rope inspection, utilising pseudo-colour imaging and maximum modulus localisation to enhance broken wire detection accuracy. Their methodology, which systematically extracts colour and texture features from MFL images, demonstrated superior portability and recognition rates compared to traditional systems, effectively reducing errors through sophisticated image enhancement techniques. Furthermore, Zhou et al. [34] engineered an integrated signal-processing method that transforms multichannel MFL signals - collected via Hall sensor arrays - into images, subsequently applying digital image processing techniques such as obliquedirectional resampling and median filtering to suppress strand and shaking noise. This comprehensive approach effectively mitigates signal attenuation and leverages multichannel fusion for noise-resilient fault diagnosis, thereby enhancing LF detection and localisation accuracy. Additionally, Liu et al. [35] implemented an advanced morphological image processing technique to convert MFL signals into images and suppress shaking noise through detailed analysis of lift-off distance and noise morphology, a method that not only reduces strand and shaking noise interference but also improves the signal-to-noise ratio for more precise defect Extending these developments, Pan et al. [36] introduced a sophisticated target-feature-oriented denoising method that enhances LF features via digital image processing to mitigate noise distortion in steel wire rope inspections, further developing a three-stage adaptive localisation framework based on disjoint region analysis to improve LF detection accuracy in denoised MFL images affected by distorted noise.

The main challenges for the reported methodologies are summarised as follows:

- (1) The detection and analysis of low-amplitude faults poses significant challenges, particularly in scenarios where signal integrity is compromised by lift-off effects or when dealing with inherently weak defect signatures. This limitation is further exacerbated in industrial environments where variable operating conditions and complex structural geometries can further attenuate already diminished signals, making reliable fault identification exceptionally challenging without specialised methodological frameworks and enhanced signal processing techniques.
- (2) Current noise reduction methodologies demonstrate critical limitations when ambient noise amplitudes approximate those of low-amplitude leakage fluxes, potentially resulting in the degradation or loss of vital fault signatures during signal processing. This challenge is particularly pronounced in industrial settings where multiple noise sources coexist, making it increasingly difficult to differentiate genuine fault signals from background interference while maintaining signal fidelity through traditional filtering approaches.
- (3) Existing localisation frameworks encounter substantial difficulties in establishing an optimal equilibrium between maximising detection accuracy and maintaining acceptable false omission rates, often resulting in procedural complexity that impacts practical implementation. This challenge is compounded by the need to process substantial volumes of data in real-time applications while ensuring reliable fault detection across varying operational conditions and defect types, necessitating more sophisticated yet efficient algorithmic approaches.

Previous research endeavours in this domain have put forth a diverse array of methodological approaches for both noise reduction and the precise localisation of LFs. Nevertheless, a particularly challenging scenario emerges when dealing with LFs of diminished magnitude, which may manifest either due to the intrinsic weakness of the LFs itself or through lift-off effects that subsequently attenuate the signal strength. Furthermore, in circumstances where the amplitude of ambient noise approximates that of these lower-magnitude LFs, conventional noise reduction techniques may inadvertently compromise the integrity of the LFs signals, thereby substantially impeding subsequent localisation procedures. Additionally, while current localisation methodologies have made significant strides, they frequently encounter difficulties in establishing an optimal equilibrium between detection accuracy and acceptable false omission rates, often resulting in procedural frameworks of considerable complexity. In response to these multifaceted challenges, this research systematically examines the distinctive characteristics of lower-amplitude LFs and proposes an innovative methodological framework designed to achieve enhanced detection rates. The fundamental scholarly contributions of this research can be delineated as follows:

- (1) A novel multi-channel magnetic signal pre-processing framework is proposed that enhances weak leakage flux signals through adaptive channel-wise feature extraction. By systematically analysing and combining complementary information from multiple magnetic sensors, this approach effectively amplifies weak damage signatures while maintaining their essential characteristics, even under challenging lift-off conditions.
- (2) An innovative scale transformation and channel fusion methodology is developed that optimally combines multi-channel magnetic leakage signals at different scales. This approach effectively suppresses environmental noise while preserving damage-related features, resulting in enhanced signal quality and improved detection capability for various types of defects in steel wire ropes.
- (3) A robust damage localisation algorithm is presented that integrates the enhanced multi-channel magnetic flux signals with optimised template matching. By leveraging the distinctive magnetic leakage patterns associated with different damage types, this method achieves superior detection accuracy and computational efficiency while maintaining low false alarm rates in steel wire rope inspection.

This research is organised into three interconnected sections that progressively build upon each other to address the challenges of defect detection in steel wire rope systems. Initially, Section 2 establishes the theoretical foundation by conducting an in-depth examination of Magnetic Flux Leakage (MFL) signal characteristics and Local Flaws (LFs) detection mechanisms, while also exploring their intricate relationships within steel wire rope infrastructures. Subsequently, Section 3 introduces and thoroughly details our novel multi-channel fusion scale transformation and signal enhancement framework, which encompasses several sophisticated components, including adaptive signal amplitude mitigation strategies, advanced contrast enhancement techniques, and innovative channel fusion methodologies that work synergistically to improve detection accuracy. The investigation culminates in Section 4, where we present an extensive experimental validation study and rigorous performance analysis that not only demonstrates the robust effectiveness of our proposed methodology in detecting and precisely localising LFs under various challenging operational conditions, but also provides detailed comparative analyses against contemporary state-of-the-art approaches to quantitatively establish the advantages of our method. Finally, Section 5 summarises the key findings, discusses the broader implications of our research, and outlines promising directions for future investigation.

2. Literature review and theoretical framework

This section presents a comprehensive examination of the existing research foundations and theoretical underpinnings that form the basis of this study. The discussion is systematically organised into two fundamental aspects: First, we explore the characteristics and behaviour of magnetic flux leakage signals in steel wire ropes (detailed in section 2.1), followed by an in-depth analysis of the distinguishing features associated with local flaws (elaborated in section 2.2). This structured approach enables a thorough understanding of both the theoretical framework and its practical applications.

2.1. Magnetic flux leakage signal characteristics in steel wire rope systems

The fundamental architectural framework of the detection apparatus is inherently rooted in Magnetic Flux Leakage (MFL) detection methodology [37], wherein the detection mechanism generates a concentrated internal magnetic field upon encircling the steel wire rope. When traversing structural irregularities, the system produces distinctive MFL signal patterns, which are systematically captured through an advanced 16-channel Hall sensor array system, enabling precise spatial localisation of Local Flaws (LFs). The Hall sensor array, strategically configured along the circumferential direction, enables quantitative measurement of radial MFL signals through the Hall effect principle, converting magnetic fluctuations into electrical signals while ensuring comprehensive rope coverage. By maintaining uniform velocity during data collection, the system achieves temporally equidistant sampling, thereby ensuring consistent data acquisition and enabling precise spatial positioning of detected flaws within the Steel Wire Rope (SWR) through sophisticated computational algorithms. Furthermore, the system's adaptability permits varying collection speeds across different processes, enhancing dataset diversity while maintaining measurement accuracy through advanced signal processing techniques and pattern recognition methodologies.

The post-acquisition processing of MFL data involves a systematic transformation of electrical signals into high-resolution images through several critical stages, ultimately achieving enhanced defect localisation precision. Initially, the trend components are methodically eliminated from the signal array, followed by the careful concatenation of 16-channel signals and their subsequent segmentation into discrete lengths of H samples. Finally, through the application of sophisticated cubic spline interpolation techniques, the resolution is substantially enhanced from 16 to K points in the channel direction, effectively transforming the extended data segments into high-fidelity $H \times K$ pixel images [36].

2.2. Characteristic features and detection mechanisms of local flaws

In the context of radial-direction MFL detection using Hall sensors, LFs exhibit distinctive signal signatures characterised by a series of adjacent peaks and valleys, occasionally manifesting with supplementary peak or valley formations [34]. This characteristic pattern has emerged as one of the most reliable and widely implemented indicators for LF detection using MFL methodology. However, it is important to note that these signal patterns are susceptible to various forms of interference, including but not limited to strand noise and mechanical vibration-induced disturbances. A particularly challenging aspect of this detection paradigm relates to the lift-off effect, which introduces multiple complexities into the detection process. This phenomenon not only exacerbates the difficulty of noise elimination but can also result in the attenuation of LF signal amplitudes, thereby significantly increasing the complexity of accurate detection and characterisation.

Contemporary research approaches have undergone a significant paradigm shift, moving away from conventional methodologies that relied on sequential denoising followed by LF detection. Instead, modern approaches directly leverage the intrinsic features of LFs, employing sophisticated template matching algorithms to identify regions exhibiting characteristic signal patterns. These advanced techniques are complemented by various threshold determination methods, ultimately enabling more precise and reliable localisation of LFs.

3. A novel framework for multi-channel fusion scale transformation and signal enhancement

This section presents a comprehensive methodological framework for multi-channel fusion scale transformation and advanced signal processing, as illustrated in Figure 1. The proposed approach systematically integrates multiple sophisticated processing stages: Initially, high-amplitude signals undergo systematic suppression through adaptive thresholding, followed by advanced contrast enhancement operations. Subsequently, the processed signals are reconstructed through innovative channel shuffling and fusion techniques, ultimately facilitating precise defect localisation through optimised brightness value analysis and spatial mapping. The transformed MFL signal scale undergoes a dual adjustment: cubic spline interpolation up-samples the original 16-channel signals to $M \times N$ dimensions, while amplitude normalisation and channel shuffle-fusion operations enhance feature-scale contrast, collectively enabling precise LF detection via integrated spatial and feature-scale transformation. This scale-driven framework is detailed in 3.1 and 3.3, where the interpolation and fusion mechanisms synergistically resolve low-amplitude defect signatures amid complex noise.

3.1. Adaptive signal amplitude mitigation and enhancement strategy

In the context of defect detection utilising Magnetic Flux Leakage (MFL) signals, the identification of low-amplitude Local Flaw (LF) signatures presents significant challenges, particularly when these signatures are situated in proximity to high-amplitude LF regions. This challenge is further compounded when the low-amplitude signals result

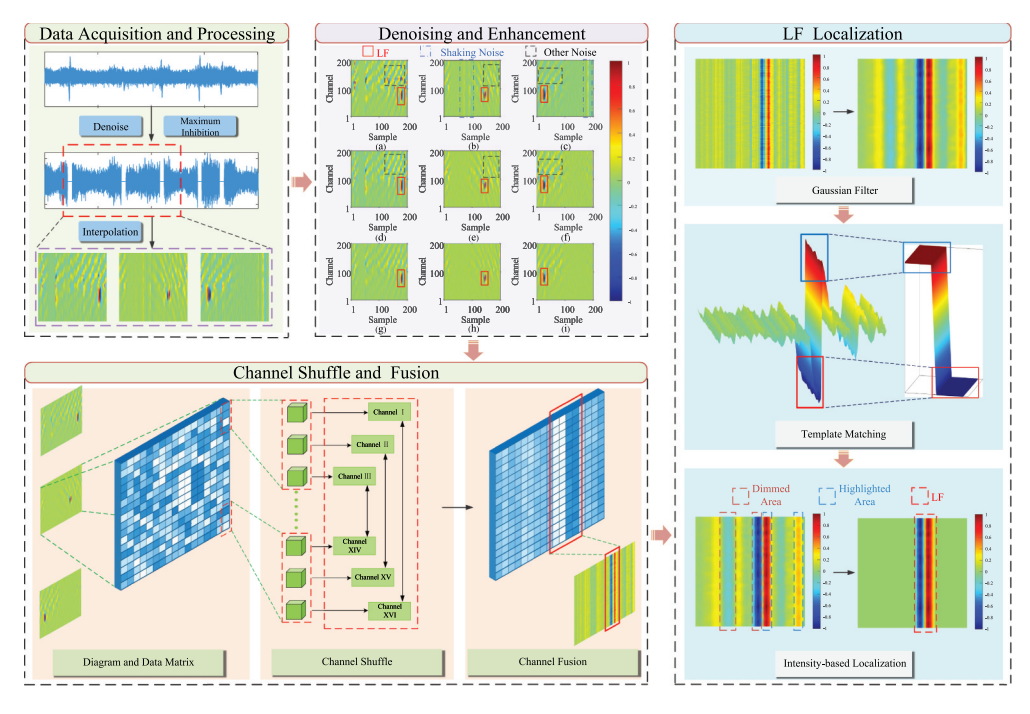


Figure 1. Architectural overview of the proposed multi-channel fusion scale transformation framework.

from either inherently smaller defects or lift-off effects [38], especially in environments characterised by strong and distorted noise patterns. Conventional threshold-based detection methodologies attempting to identify such subtle LF signatures frequently result in false positive classifications, wherein noise artefacts are erroneously identified as defect indicators. To address these limitations, our framework implements a two-stage approach: First, we establish a systematic procedure for identifying and marking the spatial coordinates of high-amplitude LF signatures, followed by selective amplitude suppression to enhance the visibility of low-amplitude features. While this methodological approach effectively enhances the prominence of smaller LF signatures, it introduces an additional technical challenge: certain noise components may exhibit amplitude characteristics that closely parallel those of the target low-amplitude LF signals. This similarity necessitates the implementation of sophisticated denoising algorithms and advanced signal differentiation methodologies, which are comprehensively detailed in subsequent sections of this analysis.

Given the original signal, defined as x[p,q] for the p-th channel at the q-th sample, where $p=1,2,\ldots,P$ and $q=1,2,\ldots,Q$, with P=16 in this implementation corresponding to the 16-channel Hall sensor array, Q depends on the length of the test SWR, the velocity during the sampling process, and the number of repetitions of the acquisition process. The signal processing procedure consists of several sequential operations, beginning with a moving average filter and culminating in matrix segmentation. Initially, a moving average filter is applied to extract the trend component, which can be expressed as:

$$a[p,q] = \frac{1}{S} \sum_{i=q-\frac{S-1}{2}}^{q+\frac{S-1}{2}} x[p,i]$$
 (1)

Subsequently, we compute the detrended signal by subtracting the trend component from the original signal:

$$b[p,q] = x[p,q] - a[p,q]$$
 (2)

where S represents the window size in the moving average filter, a[p,q] denotes the smoothed signal obtained through the application of the moving average filter to x[p,q], and b[p,q] corresponds to the detrended signal component.

Following this initial detrending step, the next processing stage implements a rigorous signal normalisation protocol. This protocol systematically maps the entire amplitude spectrum to a standardised range of [-1, 1]:

$$h[p,q] = \frac{b[p,q] - b_{\min}}{b_{\max} - b_{\min}} \times 2 - 1$$
 (3)

where h[p,q] represents the processed signal after applying the normalisation protocol, b_{\min} and b_{\max} represent the minimum and maximum values of b[p,q], respectively. This normalisation procedure reveals that, notwithstanding the presence of various high-amplitude noise components, numerous defect signatures maintain distinct identifiability, thus enabling direct localisation at the signal level, as empirically demonstrated in Figure 1. Through comprehensive empirical analysis and iterative validation, an optimal threshold value of $\tau = 0.4$ was established, achieving an optimal balance between reliable LF detection and noise rejection, whereby signal values with absolute magnitude exceeding τ are set to zero. This processed signal, denoted as y[p,q], can be formally defined as:

$$y[p,q] = \begin{pmatrix} 0 & |h[p,q]| > \tau \\ h[p,q] & \text{otherwise} \end{pmatrix}$$
 (4)

here, y[p,q] denotes the thresholded signal value for the p-th channel at the q-th sample point.

The thresholded signal matrix of dimensions $P \times Q$, we proceed to interpolate the data from the original P channels to M channels. For each sample index $q = 1, 2, \dots, Q$, the interpolation process involves the following steps:

$$\mathbf{y}_{q} = [y(1,q), y(2,q), \dots, y(P,q)]^{T}$$
 (5)

$$\xi_m = 1 + (m-1) \cdot \frac{P-1}{M-1}, \quad m = 1, 2, \dots, M$$
 (6)

$$z(m,q) = \Phi(\xi_m; \mathbf{y}_q), \quad m = 1, 2, \dots, M$$
(7)

where \mathbf{y}_q represents the column vector corresponding to sample q, ξ_m denotes the uniformly distributed interpolation points along the channel dimension within [1, P], and Φ represents the cubic spline interpolation function that estimates the signal value at ξ_m based on \mathbf{y}_a , z(m,q) represents the interpolated signal value at the m-th channel for the q-th sample.

The resulting interpolated matrix **Z** can be expressed in its complete form as:

$$\mathbf{Z} = \begin{bmatrix} z(1,1) & z(1,2) & \cdots & z(1,Q) \\ z(2,1) & z(2,2) & \cdots & z(2,Q) \\ \vdots & \vdots & \ddots & \vdots \\ z(M,1) & z(M,2) & \cdots & z(M,Q) \end{bmatrix}$$
(8)

To facilitate subsequent analysis and detection procedures, matrix **Z** is partitioned into sub-matrices of size $M \times N$, where N = M in this implementation. For each column block index $i = 1, 2, ..., \lceil \frac{Q}{N} \rceil$, the corresponding sub-matrix Z_i is extracted as:

$$Z_{i} = \begin{bmatrix} z(1, (i-1) \cdot N + 1) & z(1, (i-1) \cdot N + 2) & \cdots & z(1, \min(i \cdot N, Q)) \\ z(2, (i-1) \cdot N + 1) & z(2, (i-1) \cdot N + 2) & \cdots & z(2, \min(i \cdot N, Q)) \\ \vdots & \vdots & \ddots & \vdots \\ z(M, (i-1) \cdot N + 1) & z(M, (i-1) \cdot N + 2) & \cdots & z(M, \min(i \cdot N, Q)) \end{bmatrix}$$
(9)

where [x] denotes the ceiling function that maps \times to the smallest following integer.

3.2. Enhancement and characterization of local flaws features

The application of maximum mitigation techniques reveals previously subtle LFs; nevertheless, the persistent presence of various noise types, particularly mechanical shaking noise and lift-off effect anomalies, continues to pose significant challenges in distinguishing authentic LF signals. The pronounced shaking noise, which substantially interferes with subsequent analytical methodologies, necessitates a targeted elimination approach. Consequently, we implemented the sophisticated denoising algorithm developed by Ren [21], which, despite the presence of minor signal distortions, effectively suppresses the pervasive shaking noise across all measurement channels, as evidenced by comparative analysis before and after denoising implementation.

The quantitative efficacy of this denoising protocol is clearly demonstrated through the juxtaposition of Figure 1(a-c,d-f). Although Ren's methodology proves highly effective in eliminating prominent shaking noise, it inevitably introduces a degree of signal amplitude attenuation. This secondary effect particularly impacts the detection and differentiation of low-amplitude LFs, which inherently possess minimal signal amplitudes. These low-amplitude LFs typically exhibit several distinctive characteristics that facilitate their identification: 1) Limited channel occupation, 2) Relatively enhanced signal strength post-Maximum Mitigation, and 3) Characteristic morphology featuring closely spaced peaks and valleys, with a consistent pattern of at most one valley between adjacent peaks or one peak between adjacent valleys.

The spatial relationship between regions of extreme intensity is quantified through the Euclidean distance metric, defined as:

$$d = \sqrt{(r_{\text{max}} - r_{\text{min}})^2 + (c_{\text{max}} - c_{\text{min}})^2}$$
 (10)

where $(r_{\text{max}}, c_{\text{max}})$ and $(r_{\text{min}}, c_{\text{min}})$ represent the row and column indices corresponding to the maximum intensity point C_{max} and minimum intensity point C_{min} , respectively.

This metric provides a fundamental measure of the spatial separation between regions of contrasting brightness within the image matrix, expressed in pixel units.

The algorithm implements a distance-based decision criterion whereby the computed Euclidean distance d is compared against a predetermined threshold $\alpha = 15$. In cases where $d > \alpha$, the algorithm terminates without further modification to preserve the original image characteristics. However, when the spatial proximity criterion is satisfied (i.e. $d \le \alpha$), the algorithm proceeds to analyse circular regions of diameter D = 40 pixels centred at both extremal points. Within these regions, pixels whose intensity values fall within the interval $[\beta \cdot C_{\min}, \beta \cdot C_{\max}]$, where $\beta = 0.4$ serves as an intensity scaling parameter, are candidates for brightness adjustment. Furthermore, to ensure robust noise discrimination and maintain structural coherence, the algorithm specifically targets connected pixel clusters while excluding isolated pixels that may represent spurious noise artefacts.

The circular region $R_D(p)$ centred at point p (representing either C_{max} or C_{min}) is formally defined as:

$$R_D(p) = \{ (m, n) : || p - (m, n)||_2 \le D/2 \}$$
 (11)

where $\|\cdot\|_2$ denotes the Euclidean norm. This formulation establishes a bounded circular domain within which subsequent intensity analysis is conducted.

The subset of pixels eligible for brightness adjustment is characterised by:

$$\mathcal{A}(p) = \{ (m, n) \in R_D(p) : \beta \cdot C_{\min} \le Z_i(m, n) \le \beta \cdot C_{\max} \}$$
 (12)

where this set A(p) includes only those pixels within $R_D(p)$ whose intensity values $Z_i(m,n)$ fall within the specified range determined by the scaling factor β applied to the minimum and maximum intensity values.

To ensure structural integrity and mitigate the impact of noise, the algorithm incorporates connectivity constraints through the identification of maximal connected components. Given a binary mask B, the largest connected component $C_{\max}(B)$ is defined by:

$$C_{\max}(B) = \arg \max_{C \in C(B)} |C| \tag{13}$$

where $\mathcal{C}(B)$ represents the set of all connected components, and |C| denotes the cardinality of component C. The corresponding pixel coordinates are collected in:

$$\mathcal{P}_{\max}(B) = \{ (m, n) : (m, n) \in \mathcal{C}_{\max}(B) \}$$

$$\tag{14}$$

The final brightness adjustment transformation is implemented through the following piecewise function:

$$Z_o(m,n) = \begin{pmatrix} 2 \cdot Z_i(m,n) & (m,n) \in \mathcal{P}_{\max}(H) \cup \mathcal{P}_{\max}(L) \\ Z_i(m,n) & \text{otherwise} \end{pmatrix}$$
(15)

where $Z_i(m,n)$ and $Z_o(m,n)$ denote the intensity values at pixel coordinates (m,n) for the input and output images, where H and L denote binary masks corresponding to highintensity and low-intensity regions, respectively. This transformation selectively doubles the intensity of pixels belonging to the largest connected components while preserving the original values of non-selected pixels, thereby maintaining the image's structural integrity while enhancing local contrast.

3.3. Channel Shuffle and fusion

While the preceding contrast enhancement phase has successfully amplified the visibility of structural defects within the image, the persistent presence of distorted strand noise coupled with subtle mechanical vibration-induced artefacts necessitates the implementation of a more sophisticated localisation methodology. To address these challenges comprehensively, this paper introduces an innovative approach incorporating channel shuffling and reconstruction mechanisms, specifically designed to mitigate the impact of these traditionally intractable noise patterns, thereby facilitating more robust defect detection. Building upon the theoretical framework established by Zhou et al. [34] in Section 2, the initially acquired 16-channel electromagnetic signals undergo a systematic process of interpolation and segmentation. This process effectively partitions the comprehensive signal into a sequence of $M \times N$ pixel images, substantially enhancing the spatial resolution of the acquired data. Each resultant image can be mathematically conceptualised as a $M \times N$ matrix, wherein individual pixel intensity values correspond directly to matrix elements. In this configuration, each row represents a distinct channel, while columns correspond to sequential samples. The physical position of these samples on the SWR depends on the inspection velocity during each detection cycle.

The proposed methodology implements a novel channel fusion approach wherein each row of the numerical matrix undergoes multiple iterations of random permutations. The cumulative results of these successive permutations are systematically integrated to achieve optimal channel fusion and reconstruction, as comprehensively illustrated in Figure 1. Empirical observations demonstrate that post-Channel Shuffle and Fusion processing, the characteristic features of LFs exhibit notably improved spatial distribution across all channels, manifesting as well-defined peaks and valleys, while simultaneously achieving significant attenuation of random noise components, thereby substantially reducing the complexity of subsequent identification procedures.

$$Z_{o} = \begin{bmatrix} a_{11} & a_{12} & \cdots & a_{1,N} \\ a_{21} & a_{22} & \cdots & a_{2,N} \\ \vdots & \vdots & \ddots & \vdots \\ a_{M,1} & a_{M,2} & \cdots & a_{M,N} \end{bmatrix}$$

$$(16)$$

Consider the matrix Z_o of dimension $M \times N$, where each element a_{ij} represents a distinct feature coefficient. In order to enhance the robustness of our analysis and mitigate the effects of localised anomalies, we implement a systematic permutation procedure. Specifically, for each row i, we apply independent random permutations P_i to generate a new matrix $Z_{o'}$, as illustrated below:

$$Z_{o}^{(k)} : \underbrace{\begin{bmatrix} a_{11} & a_{12} & \dots & a_{1,N} \\ a_{21} & a_{22} & \dots & a_{2,N0} \\ \vdots & \vdots & \ddots & \vdots \\ a_{M,1} & a_{M,2} & \dots & a_{M,N} \end{bmatrix}}_{\text{Original Matrix } Z_{o}} \xrightarrow{P_{i}} \underbrace{\begin{bmatrix} a'_{11} & a'_{12} & \dots & a'_{1,N} \\ a'_{21} & a'_{22} & \dots & a'_{2,N} \\ \vdots & \vdots & \ddots & \vdots \\ a'_{M,1} & a'_{M,2} & \dots & a'_{M,N} \end{bmatrix}}_{\text{Permuted Matrix } Z_{o}^{(k)}}$$

$$(17)$$

Subsequently, this permutation process is iterated j times, yielding a sequence of matrices $Z_o^{(k)}$ for k = 1, 2, ..., j. These matrices are then aggregated through summation to produce the final fusion matrix:

$$I = Z_{\text{fusion}} = \sum_{k=1}^{j} Z_o^{(k)}$$
 (18)

Through this iterative permutation and aggregation process, the resultant matrix $I = Z_{\text{fusion}}$ demonstrates notably improved characteristics, particularly in terms of the spatial distribution of LFs. Moreover, this methodology effectively attenuates random noise components while preserving the essential structural information, thereby enhancing the reliability and interpretability of the feature representation.

3.4. Localization of local flaws through template matching analysis

This critical stage implements a sophisticated dual-approach methodology, combining template matching techniques with mean brightness value analysis to precisely determine the spatial coordinates of LFs within the target image. The process begins with the application of Gaussian filtering as a preliminary preprocessing step, which serves to enhance image smoothness and amplify the contrast between distinct brightness regions, thereby establishing a more robust foundation for subsequent analytical procedures.

Following this initial pre-processing phase, the algorithm proceeds with a template-based analysis that accounts for the inherent binary nature of LF manifestations. Given that LFs characteristically present themselves as either a light-to-dark or dark-to-light transition region, the methodology necessitates the implementation of two complementary symmetric templates to comprehensively capture these bidirectional variations. In accordance with the dimensional constraints established in Section 3.3, these templates must maintain a vertical dimension of H (where H = M by definition), while the horizontal extent of each brightness region typically encompasses approximately W units, with an additional unit-width transition zone to accommodate gradual brightness variations. These geometric and photometric requirements can be formally expressed through the following matrix representations:

$$Template1 = \begin{bmatrix} 1 & \cdots & 1 & 0 & -1 & \cdots & -1 \\ \vdots & \ddots & \vdots & \vdots & \vdots & \ddots & \vdots \\ 1 & \cdots & 1 & 0 & -1 & \cdots & -1 \end{bmatrix}_{H \times (2W+1)} = \begin{bmatrix} \mathbf{1}_{W} & 0 & -\mathbf{1}_{W} \\ \vdots & \vdots & \vdots \\ \mathbf{1}_{W} & 0 & -\mathbf{1}_{W} \end{bmatrix}_{H \times (2W+1)}$$
(19)

$$\text{Template2} = \begin{bmatrix} -1 & \cdots & -1 & 0 & 1 & \cdots & 1 \\ \vdots & \ddots & \vdots & \vdots & \vdots & \ddots & \vdots \\ -1 & \cdots & -1 & 0 & 1 & \cdots & 1 \end{bmatrix}_{H \times (2W+1)} = \begin{bmatrix} -\mathbf{1}_{W} & 0 & \mathbf{1}_{W} \\ \vdots & \vdots & \vdots \\ -\mathbf{1}_{W} & 0 & \mathbf{1}_{W} \end{bmatrix}_{H \times (2W+1)}$$
(20)

For the implementation of template matching, I represents the matrix obtained from the process described in Section 3.3, with dimensions $M \times N$, this matrix denotes the input image for subsequent processing and analysis. And let T_1 and T_2 denote the respective template matrices, each sized $H \times (2W+1)$. The methodology employs Normalized Cross-Correlation (NCC) as the primary matching metric, chosen for its robustness to intensity variations and superior performance in pattern recognition tasks. The NCC computation is formally defined as:

$$C_{T_p}(m,n) = \frac{\sum_{i=0}^{H-1} \sum_{j=0}^{2W} (I(m+i,n+j-W) - \overline{I_{mn}}) (T_p(i,j) - \overline{T}_p)}{\sqrt{\sum_{i=0}^{H-1} \sum_{j=0}^{2W} (I(m+i,n+j-W) - \overline{I_{mn}})^2} \cdot \sqrt{\sum_{i=0}^{H-1} \sum_{j=0}^{2W} (T_p(i,j) - \overline{T}_p)^2}}$$
(21)

In this formulation, $C_{T_p}(m,n)$ represents the normalised correlation coefficient between template T_p and the corresponding local region within image I at coordinates (m,n). The terms $\overline{I_{mn}}$ and \overline{T}_p denote the mean values of the local image region and template, respectively, ensuring normalisation across varying brightness conditions.

The correlation results undergo systematic binary classification through a threshold-based discrimination process, which can be formally expressed as:

$$B_p(m,n) = \begin{pmatrix} 1 & C_{T_p}(m,n) \ge \mu \\ 0 & \text{otherwise} \end{pmatrix}$$
 (22)

where μ represents a carefully calibrated threshold parameter that discriminates between significant and insignificant correlation responses. The resulting binary map $B_p(m,n)$ maintains dimensional consistency with the original input matrix I. The final detection map is synthesised through the logical fusion of both template responses, effectively capturing all potential LF manifestations regardless of their orientation.

$$B(m,n) = B_1(m,n) \vee B_2(m,n)$$
 (23)

Following the implementation of dual-template matching for initial LF localisation and considering the aforementioned preprocessing steps, it becomes feasible to exploit the intrinsic brightness characteristics of the regions of interest. Notably, in the absence of Channel Shuffle and Fusion operations, the precise determination of the LF's dimensional parameters (width, height) and channel positions within the image matrix remains ambiguous, consequently leading to computationally intensive operations and diminished verification accuracy. However, the preliminary processing framework enables the optimal utilisation of average brightness analysis. This methodology encompasses the systematic partitioning of the image into fixed-width regions, followed by the computation and hierarchical ranking of regional brightness averages, ultimately facilitating the identification of regions exhibiting extreme brightness values and their spatial relationships. The integration of this brightness-based analysis with the previously identified high-response regions from template matching enables a comprehensive evaluation framework for definitive LF position determination through intersection analysis.

Given the input image matrix I, the systematic regional partitioning and subsequent average brightness computation can be mathematically expressed as:

$$A_t = \frac{1}{W \cdot M} \sum_{i=0}^{M-1} \sum_{j=0}^{W-1} I(i, j + kW)$$
 (24)

where W represents the width of the sliding window operator, and A_t denotes the average brightness value computed for the t-th region, initiating at column tW and extending over W columns. Subsequently, the algorithm performs a comprehensive sorting operation on the set of average brightness values A_t to identify the k highest and lowest intensity regions, denoted as sets H_k and L_k respectively. The methodology specifically considers regions within H_k and L_k that exhibit spatial overlap or adjacency as potential LF positions, formally defined as A(m, n), where m and n represent the respective row and column indices.

The final LF localisation result is achieved through the logical integration of both detection methodologies, formally defined as:

$$F(m,n) = A(m,n) \wedge B(m,n) \tag{25}$$

where F(m, n) represents the definitive spatial location of the LF within the image matrix.

4. Experimental validation and performance analysis

This section presents a comprehensive validation and rigorous experimental analysis of the Multi-Channel Fusion Scale Transformation (MCFST) method's effectiveness, focusing particularly on its capabilities in detecting and characterising challenging Local Flaws (LFs) that manifest with lower amplitude signatures. Furthermore, the validation process encompasses both quantitative and qualitative assessments to establish the method's

```
Algorithm 1 Multi-channel Fusion Scale Transformation (MCFST) for Local Flaw Detection
 1: procedure Signal Preprocessing(Raw MFL signal x[p,q], P=16 channels, Q samples)
 2:
       Input parameters:
 3:
       S: window size for moving average filter
 4:
       \tau: amplitude suppression threshold (e.g. 0.4)
       M, N: dimensions for interpolation and segmentation (M = N = 200)
 5:
 6:
       \alpha: Euclidean distance threshold (e.g. 15)
 7:
       \beta: intensity scaling factor (e.g. 0.4)
       for p = 1 to P do
 8:
           for q = 1 to Q do
 9:
              Calculate moving average: a[p,q] = \frac{1}{S} \sum_{i=q-\frac{S-1}{2}}^{q+\frac{S-1}{2}} x[p,i]
10:
              Detrend signal: b[p,q] = x[p,q] - a[p,q]
11:
12:
13.
       end for
14:
       Output: Normalized signal matrix h[p,q]
15: end procedure
16: procedure Signal Enhancement(Matrix Z)
       for i = 1 to \lceil \frac{Q}{N} \rceil do
17:
18:
           Extract submatrix Z_i = Z[:, (i-1)N + 1 : \min(iN, Q)]
19:
           Compute Euclidean distance d between max/min intensity points
20:
21:
               Enhance brightness in regions RD(C_{max}), RD(C_{min})
22:
           end if
23:
       end for
       Output: Enhanced matrix Z_o
24:
25: end procedure
26: procedure FLAWLOCALIZATION(Binary map B(m, n), Enhanced matrix Z_o)
       Compute average brightness A_t for width-W regions
27:
28:
       Generate candidate map A(m, n)
       Final detection: F(m,n) = A(m,n) \wedge B(m,n)
29:
30:
       Output: Local Flaw location map F(m, n)
31: end procedure
```

robustness and reliability under various operational conditions simulating critical industrial field inspection scenarios, including variable operational speeds, circumferential orientations, and controlled jitter. Additionally, through systematic investigation and comparative analysis with conventional detection approaches, this study demonstrates how the MCFST method addresses the longstanding challenges associated with weak signal detection in Steel Wire Rope (SWR) inspection systems across diverse applications like elevators, mining equipment, and bridges. Moreover, the experimental framework incorporates multiple test scenarios and environmental variables specifically designed to simulate real-world challenges such as lift-off effects and complex noise environments to ensure comprehensive evaluation of the method's performance in real-world applications, thereby providing substantial evidence for its practical utility in industrial deployment. The subsequent analysis not only validates the theoretical foundations of the MCFST approach but also establishes its superiority in enhancing the detection sensitivity and accuracy for subtle structural anomalies that have traditionally posed significant challenges in non-destructive testing protocols.

The MFL detection method for SWRs functions by identifying magnetic field anomalies at defect locations within magnetised ropes. The detection system employs Hall sensors to pinpoint these defect positions with precision. As illustrated in Figure 2(a), the detector comprises a sensor system architecture that includes two concentric permanent ring magnets with radial magnetisation, magnetic yokes, and sensor arrays. The magnetisation system incorporates these custom-engineered ring magnets and yoke magnetic bridges that encircle the SWR, establishing a magnetic circuit that drives the rope to magnetic saturation. This saturation condition is crucial for generating detectable MFL signals at defect sites. The test rig configuration, shown in Figure 2(b), reveals the internal sensor arrangement consisting of two semicircular PCB circuit boards equipped with 16 uniformly distributed Hall sensors spaced at 22.5° intervals to capture radial MFL signals. During operation, analog voltage outputs from the Hall sensor array are digitised in realtime by a 16-bit analog-to-digital converter with 5 V dynamic range. The digitised multichannel data is streamed to an embedded computing unit where axial position is synchronised with encoder pulses to correlate temporal signals with spatial coordinates along the rope's longitudinal axis. The experimental setup utilises two test specimens: a 32mm diameter SWR and a 30mm diameter SWR, each containing four artificially created broken wire LFs. These manufactured defects vary in severity, spanning from single wire breaks to 3.5 broken wires, providing a range of test conditions for system validation. The practical inspection scenarios, as depicted in Figure 2(c), demonstrate the field deployment of the MFL test rig.

In the context of rigorous field testing protocols, the MFL acquisition process is meticulously controlled through three critical operational variables: the detector's longitudinal movement speed along the SWR, its precise circumferential orientation relative to the rope's central axis, and the frequency of intentionally induced rope jittering. To systematically evaluate the system's performance across a spectrum of inspection velocities, the detector is operated at three carefully selected speeds – 0.5 m/s, 1 m/s, and 1.5 m/s - while maintaining consistent measurement parameters. Furthermore, the circumferential orientation is methodically controlled by rotating the detector around the SWR's circumference, whereby measurements are acquired at precise 30 intervals, thus generating 12 comprehensive datasets that collectively encompass the rope's entire

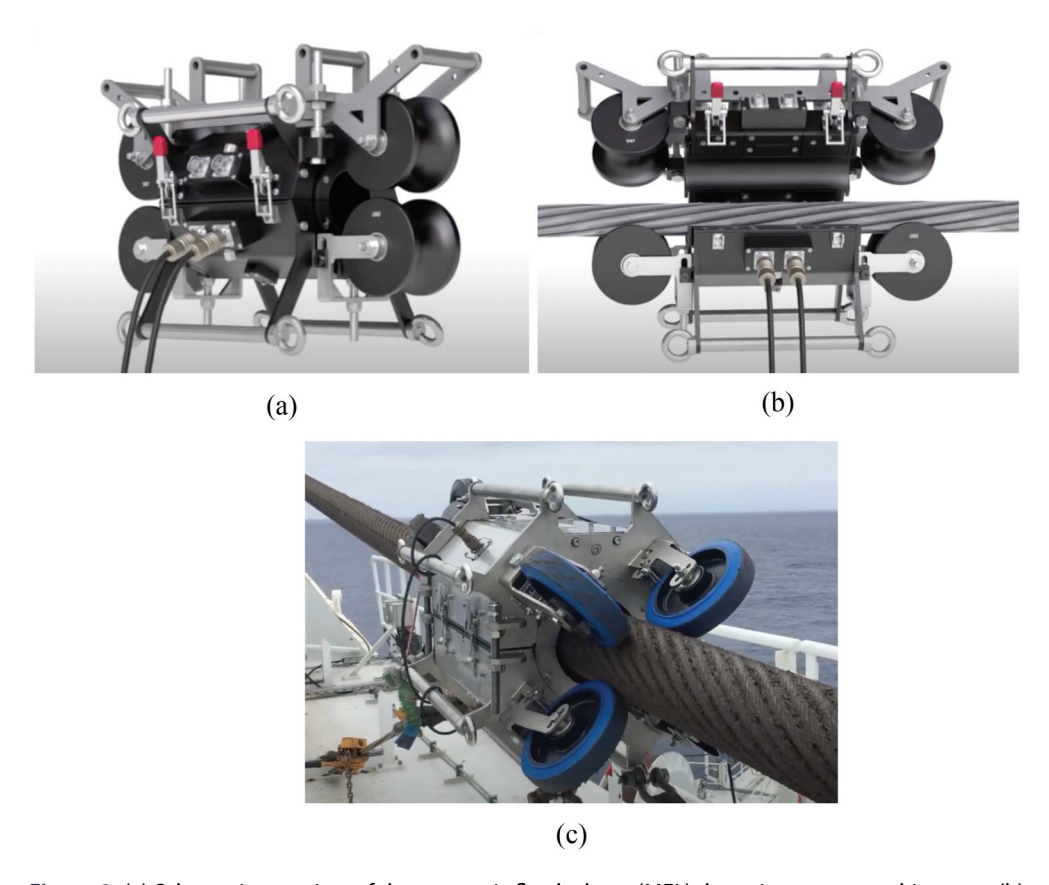


Figure 2. (a) Schematic overview of the magnetic flux leakage (MFL) detection system architecture, (b) detailed view of the MFL test rig configuration showing internal sensor arrangement, (c) field deployment of the MFL test rig during practical inspection scenarios.

circumferential profile. Additionally, to simulate various real-world vibration conditions that may be encountered during actual inspections, rope jittering is systematically tested across a controlled frequency range spanning from 0 to 3. It should be noted that to ensure comprehensive data collection, we also test speeds at 0.1 m/s increments around each baseline value (0.5 m/s, 1 m/s, and 1.5 m/s) and systematically sample jitter frequencies at 0.5 intervals across the entire 03 range. This approach will provide a more complete understanding of the system's performance under varied operating conditions.

Table 1 provides comprehensive visual documentation and systematic severity classification of structural damage patterns observed in the SWR specimens, whereby each specimen consistently manifests two distinct LFs. The primary defect is predominantly characterised by severe structural deterioration, which encompasses either complete wire breakage or substantial cross-sectional reduction, whereas the secondary defect exhibits relatively milder forms of degradation. In order to rigorously validate the experimental findings and establish robust correlations, we conducted detailed analyses of three characteristic signal segments, with each segment containing 200 discrete sampling points (although it should be noted that due to inherent variations in data collection speeds, the physical distances represented by these sample points may exhibit some variability across

Table 1. Specifications of the LFs.

No.	LF1	Length of the LF	LF2	Length of the LF
1		5mm		3 mm
2		3mm		5 mm
3		4.5mm		3 mm

different datasets), as comprehensively illustrated in Figure 3(a) through (c). Furthermore, these carefully selected signal segments demonstrate direct and unambiguous correspondence to the three distinct damage configurations meticulously documented in Table 1, thereby establishing a clear and quantifiable relationship between the observed physical damage patterns and their associated electromagnetic signal responses. Through the application of the transformation algorithms defined in Eq.(5) \sim (7), these temporal signals were subsequently converted into two-dimensional spatial representations with dimensions of 200 \times 200 pixels, as illustrated in Figure 3(d-f).

Critical examination of the three signal segments reveals that each contains a prominent LF signature with substantial amplitude, accompanied by an adjacent, significantly attenuated LF signal. Conventional detection methodologies frequently fail to identify these lower-amplitude anomalies due to their diminished signal strength. To address this limitation, we implemented Maximum Mitigation preprocessing on the dominant amplitude signals according to Equation (3~4), with results demonstrated in Figure 4(a-c). While this procedure successfully amplifies the LF signatures, it concurrently increases the noise floor, necessitating additional signal-to-noise ratio enhancement.

Analysis of Figure 4(a-c) reveals distinct characteristic differences between LF signatures and noise components. LF signals consistently exhibit greater amplitude magnitude and demonstrate spatial continuity and adjacency, whereas noise components lack these defining characteristics. Leveraging these discriminative features through the application of Equation (10-15), we achieved enhanced LF signal definition while preserving original noise characteristics, as illustrated in Figure 4(d-f). This enhancement significantly

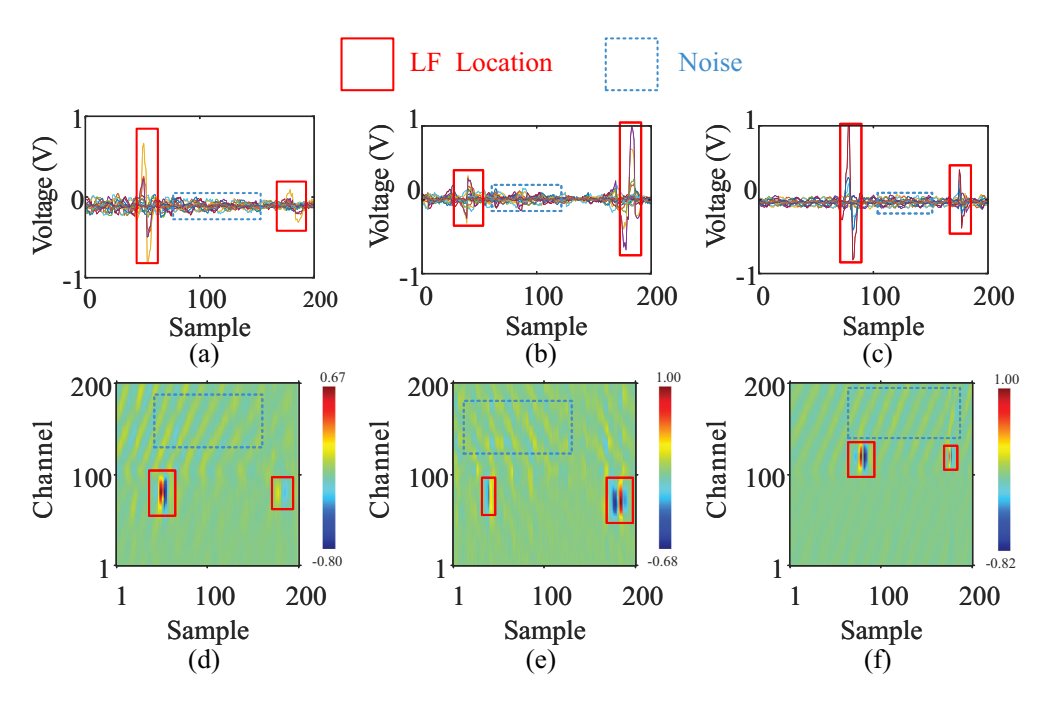


Figure 3. Comparative visualization of signal transformation: (a) \sim (c) original MFL signals containing dual LF signatures; (d) \sim (f) corresponding interpolated image representations.

improves the signal-to-noise contrast ratio, thereby facilitating subsequent processing and precise LF localisation.

The final stage implements Channel Shuffle and Fusion operations according to Equation (10-18). Comparative analysis between Figure 4(d-f,g-i) demonstrates the efficacy of this approach. Through this process, LF signatures achieve uniform distribution across all channels, substantially minimising noise interference and enabling simplified defect localisation methodologies in subsequent processing stages.

Following the multi-channel processing stages, precise LF localisation is executed utilising Eq. (21) through Eq. (25). Subsequently, the spatial coordinates of the previously identified and Mitigated LF signals are systematically mapped onto the resultant image. This comprehensive approach facilitates the accurate identification of all LF features, with the final localisation outcomes clearly demonstrated in Figure 5(d1) through (d3).

To rigorously evaluate and validate the effectiveness of our proposed methodology, we conducted extensive comparisons against three widely-adopted LF detection approaches: the Canny Edge Detection (CED) algorithm [32], the Constant Threshold (CT) method [35], and the Adaptive Threshold (AT) technique [36]. For the three distinct signal segments illustrated in Figure 3, we initially applied the target-feature-oriented denoising method [36] to enhance the signal quality prior to final localisation using the aforementioned three methods. While both the Canny Edge Detection and Constant Threshold methods successfully identified all LF features, they simultaneously generated substantial false positives, thereby significantly compromising the reliability of actual defect identification, as evidenced in Figure 5(a1) through (b3). Although the Adaptive Threshold method generally demonstrates superior robustness under standard conditions, it

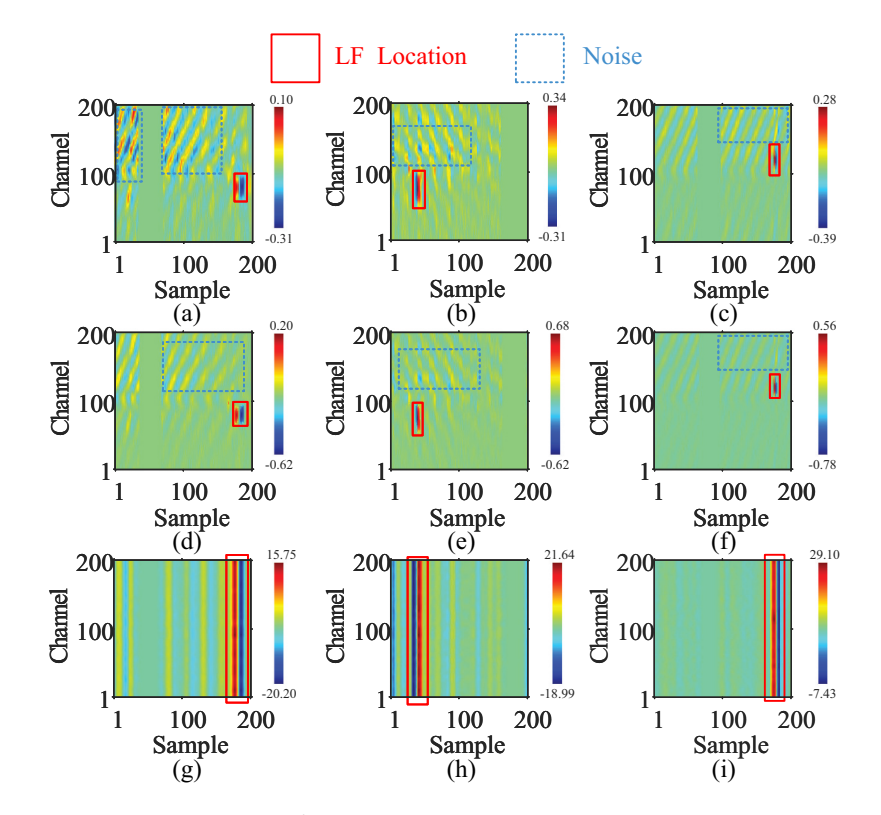


Figure 4. Systematic visualization of the experimental processing procedure. (a)~(c) post-maximum mitigation processed images. (d) \sim (f) images following low-frequency feature enhancement. (g) \sim (i) results after Channel Shuffle and feature fusion operations.

exhibits notable limitations when confronted with scenarios involving small-amplitude LF defects adjacent to large-amplitude ones, frequently failing to detect the smaller defects, as shown in Figure 5(c1) through (c3). In contrast, our proposed method effectively addresses these limitations, achieving precise defect localisation while minimising false positives, as depicted in Figure 5(d1) through (d3).

In order to validate the practical effectiveness of our proposed methodology, we conducted comprehensive performance testing by processing three distinct signal segments, which are illustrated in Figure 4(a-c), through our detection framework. The experimental computations were executed on a standardised testing platform that consisted of an Intel Core i5-9300 H processor operating at 2.40-GHz, complemented by 16 GB of system memory, and running under the Windows 11 64-bit operating environment. The computational analysis revealed that the processing durations required to generate the detection outcomes, as depicted in Figure 5(d1-d3), were 0.51 seconds, 0.73 seconds, and 0.61 seconds respectively, yielding an average processing time of approximately 0.62 seconds per signal segment. These empirical results demonstrate that our method exhibits robust computational efficiency, thereby making it particularly suitable for real-world implementations, especially considering that the processing performance could be further enhanced through the utilisation of more sophisticated hardware configurations or parallel processing architectures.

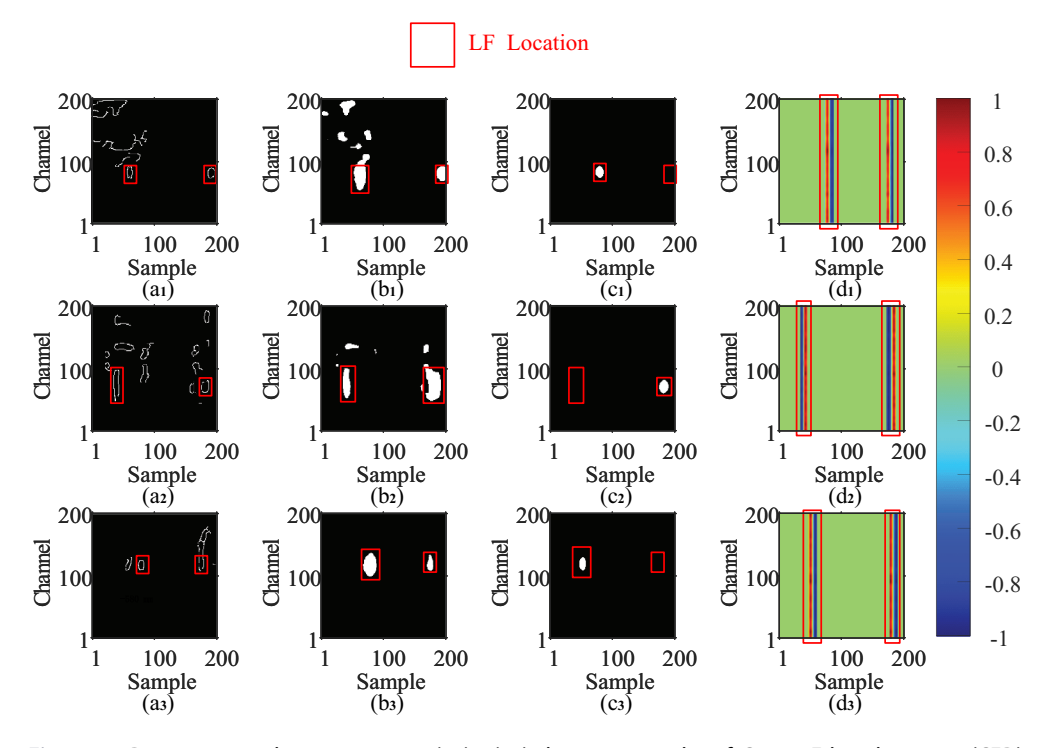


Figure 5. Detection results comparison. (a1) \sim (a3) detection results of Canny Edge detection (CED) algorithm method. (b1) \sim (b3) detection results of Constant Threshold (CT) method. (c1) \sim (c3) detection results adaptive Threshold (AT) method.(d1) \sim (d3) detection results of proposed multi-channel fusion scale transformed (MCFST) method.

To ensure a comprehensive and statistically significant evaluation, we utilised an extensive dataset comprising multiple signal segments containing 764 LF features. The comparative analysis of detection performance across all four methods is meticulously documented in Table 2 and visualised in Figure 6. The quantitative assessment reveals that while the Canny Edge Detection and Constant Threshold methods achieve reasonable detection rates, they are significantly compromised by excessive false positives, with the former generating an unprecedented 5865 false detections. The Adaptive Threshold method demonstrates markedly improved false positive control, recording only 80 such instances, though maintaining room for optimisation across all performance metrics. Our proposed methodology achieves superior results, successfully identifying 748 true positives while maintaining minimal false positives and negatives.

The performance metrics – Precision, Recall, and F1 score – were calculated to provide a holistic evaluation of detection efficacy. These metrics, visualised in Figure 7, demonstrate the substantial advantages of our proposed approach. While the Canny Edge Detection method's extremely low precision results in an F1 score of merely 0.1548, and the Constant Threshold method achieves a modest 0.4512, the Adaptive Threshold method shows significant improvement with an F1 score of 0.9152. Notably, our proposed methodology achieves the highest F1 score of 0.9765, substantiating its superior comprehensive performance across all evaluation metrics.

Table 2. Quantitative performance assessment of different methods.

Performance metrics	CED method	CT method	AT method	MCFST method
Number of true positives	513	733	712	748
Number of false positives	5863	1752	80	20
Number of false negatives	251	31	52	16
Precision	8.75%	29.50%	89.90%	97.40%
Recall	67.15%	95.94%	93.19%	97.91%
F1 score	0.1548	0.4512	0.9152	0.9765

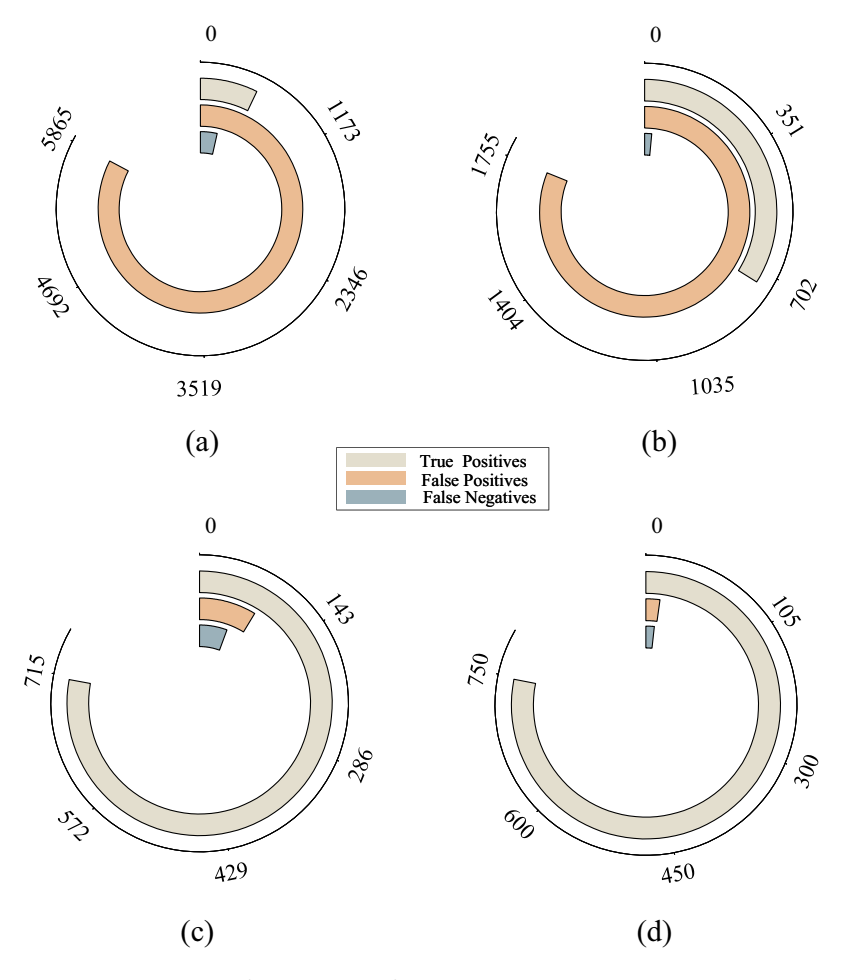


Figure 6. Quantitative analysis of detection performance metrics across methodologies. (a) Statistical distribution of true positives (TP), false positives (FP), and false negatives (FN) using Canny Edge detection (CED) algorithm. (b) Detection performance metrics utilizing Constant Threshold (CT) methodology. (c) Statistical outcomes from adaptive Threshold (AT) implementation. (d) Comprehensive detection metrics achieved through the proposed multi-channel fusion scale transformed (MCFST) method.

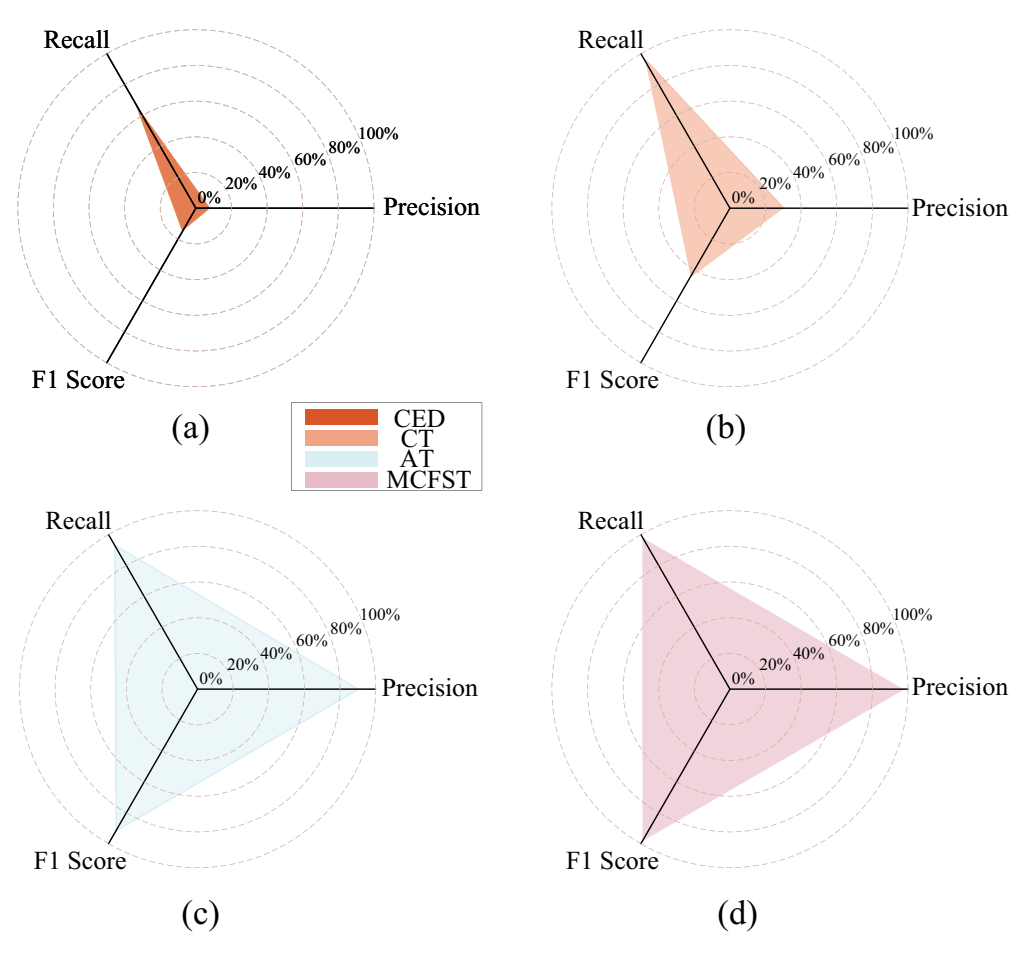


Figure 7. Multi-dimensional performance evaluation using radar chart visualization. (a) Triaxial representation of precision, recall, and F1 score for Canny Edge detection (CED) implementation. (b) Performance metric distribution for Constant Threshold (CT) methodology. (c) Three-dimensional performance analysis of adaptive Threshold (AT) approach. (d) Comprehensive performance metrics demonstration of the proposed multi-channel fusion scale transformed (MCFST) methodology, highlighting superior detection capabilities.

5. Conclusion

This research has successfully developed and validated a novel multi-channel fusion scale transformation approach for detecting and localising Local Faults in Steel Wire Rope systems. The innovative three-fold framework proposes morphological signal enhancement, introduces an advanced Channel Shuffle and Fusion mechanism, and implements template matching with luminance characteristics, demonstrating exceptional capabilities in addressing critical challenges in non-destructive testing. Experimental results confirm the method's superior performance in detecting diminished-magnitude faults under challenging conditions, while maintaining computational efficiency. These newly proposed techniques provide a robust foundation for early fault detection across various industrial applications, significantly advancing the field of structural health monitoring.

However, while demonstrating significant advancements, the proposed method has several inherent limitations. The effectiveness depends heavily on the multichannel Hall sensor array configuration, and residual noise components may still affect detection accuracy in extremely noisy operating conditions. Parameter tuning is required for different rope specifications, while signal processing may occasionally mask subtle fault indicators. Future work should focus on developing adaptive thresholding techniques, integrating machine learning for enhanced defect classification, validating the method's efficacy for Loss of Metallic Area (LMA) and single broken wire defects, and optimising computational efficiency for real-time applications.

Disclosure statement

No potential conflict of interest was reported by the author(s).

Funding

This research was supported by the National Natural Science Foundation of China [Grants 52105111 and 52305085], the Guangdong Basic and Applied Basic Research Foundation [Grant 2025A1515012256], the Shantou University (STU) Scientific Research Initiation Grant [NTF21029], the Nuclear Power Institute of China Original Foundation [Grant KJCX2022YC111], the Natural Science Foundation of Sichuan Province [Grant 2023NSFSC0861], the China Postdoctoral Science Foundation [Grant 2023M740021], the Natural Science Foundation of Anhui Province [Grant 2108085QE229], the Industry-Academia Cooperation Project from the Guangdong Institute of Special Equipment Inspection and Research Shunde Branch [XTJ-KY01-202503-030], and the Enterprise Collaboration Project from the National Excellent Engineer Innovation Research Institute for Advanced Manufacturing Industry in Foshan of Guangdong-Hong Kong-Macao Greater Bay Area [NSJH2025008].

References

- [1] Mazurek P. A comprehensive review of steel wire rope degradation mechanisms and recent damage detection methods. Sustainability. 2023;15(6):5441. doi: 10.3390/su15065441
- [2] Peterka P, Krešák J, Kropuch S, et al. Failure analysis of hoisting steel wire rope. Eng Fail Anal. 2014;45:96–105. doi: 10.1016/j.engfailanal.2014.06.005
- [3] Zhou P, Zhou G, Zhu Z, et al. A review of non-destructive damage detection methods for steel wire ropes. Appl Sci. 2019;9(13):2771. doi: 10.3390/app9132771
- [4] Chen P, Zhang R, He C, et al. Progressive contrastive representation learning for defect diagnosis in aluminum disk substrates with a bio-inspired vision sensor. Expert Syst Appl. 2025;289:128305. doi: 10.1016/j.eswa.2025.128305
- [5] Chen P, Ma J, He C, et al. Semi-supervised consistency models for automated defect detection in carbon fiber composite structures with limited data. Meas Sci Technol. 2025;36(4):046109. doi: 10.1088/1361-6501/adc031
- [6] Farhidzadeh A, Salamone S. Reference-free corrosion damage diagnosis in steel strands using guided ultrasonic waves. Ultrasonics. 2015;57:198–208. doi: 10.1016/j.ultras.2014.11. 011
- [7] Chen P, Zhang R, Fan S, et al. Step-wise contrastive representation learning for diagnosing unknown defective categories in planetary gearboxes. Knowl-Based Syst. 2024;309:112863. doi: 10.1016/j.knosys.2024.112863



- [8] Rostami J, Tse PW, Yuan M. Detection of broken wires in elevator wire ropes with ultrasonic guided waves and tone-burst wavelet. Struct Health Monit. 2020;19(2):481-494. doi: 10.1177/1475921719855915
- [9] Chen P, Gao J, Zhang R, et al. Metric-guided graph contrastive learning: an unsupervised approach for few-shot gearbox fault diagnosis. Meas Sci Technol. 2025;36(7):076110. doi: 10.1088/1361-6501/ade7a7
- [10] Chen P, Wu Y, Xu C, et al. Interference suppression of nonstationary signals for bearing diagnosis under transient noise measurements. IEEE Trans Rel. 2025:1-15. doi: 10.1109/TR. 2025.3527739
- [11] Chen P, Wu Y, Fan S, et al. Adaptive signal regime for identifying transient shifts: a novel approach toward fault diagnosis in wind turbine systems. Ocean Eng. 2025;325:120798. doi: 10.1016/j.oceaneng.2025.120798
- [12] Dong Y, Pan Y, Wang D, et al. Corrosion detection and evaluation for steel wires based on a multi-vision scanning system. Construct Building Mater. 2022;322:125877. doi: 10.1016/j. conbuildmat.2021.125877
- [13] Zhou P, Zhou G, Wang H, et al. Intelligent visual detection method for the early surface damage of mine hoisting wire ropes. Meas Sci Technol. 2024;35(11):115018. doi: 10.1088/ 1361-6501/ad6a78
- [14] Chen P, Ma Z, Xu C, et al. Self-supervised transfer learning for remote wear evaluation in machine tool elements with imaging transmission attenuation. IEEE Internet Things J. 2024;11(13):23045-23054. doi: 10.1109/JIOT.2024.3382878
- [15] Schaal C, Bischoff S, Gaul L. Damage detection in multi-wire cables using guided ultrasonic waves. Struct Health Monit. 2016;15(3):279-288. doi: 10.1177/1475921716642747
- [16] Raišutis R, Kažys R, Mažeika L, et al. Ultrasonic guided wave-based testing technique for inspection of multi-wire rope structures. NDT E Int. 2014;62:40-49. doi: 10.1016/j.ndteint. 2013.11.005
- [17] Zhang G, Tang Z, Fan Y, et al. Steel wire rope surface defect detection based on segmentation template and spatiotemporal gray sample set. Sensors. 2021;21(16):5401. doi: 10.3390/
- [18] Huang X, Liu Z, Zhang X, et al. Surface damage detection for steel wire ropes using deep learning and computer vision techniques. Measurement. 2020;161:107843. doi: 10.1016/j. measurement.2020.107843
- [19] Liu S, Sun Y, Kang Y. A novel e-exponential stochastic resonance model and weak signal detection method for steel wire rope. IEEE Trans Ind Electron. 2021;69(7):7428-7440. doi: 10.1109/TIE.2021.3095802
- [20] Zhang D, Zhang E, Pan S. A new signal processing method for the nondestructive testing of a steel wire rope using a small device. NDT E Int. 2020;114:102299. doi: 10.1016/j.ndteint.
- [21] Ren L, Liu Z, Zhou J. Shaking noise elimination for detecting local flaw in steel wire ropes based on magnetic flux leakage detection. IEEE Trans Instrum Meas. 2021;70:1-9. doi: 10. 1109/TIM.2021.3112792
- [22] Chen P, Ma Z, Xu C, et al. Scale-aware domain adaptation for surface defects detection on machine tool components in contaminant measurements. IEEE Trans Instrum Meas. 2025;74:1-9. doi: 10.1109/TIM.2024.3502888
- [23] Pan F, Huang Y, Ren L, et al. Inspection of wire ropes based on magnetic flux leakage images by using YOLOv5. In: 2023 Global Reliability and Prognostics and Health Management Conference (PHM-Hangzhou), Hangzhou, China: IEEE; 2023. p. 1-7. doi: 10.1109/PHM-Hangzhou58797.2023.10482526.
- [24] Chen P, Xu C, Ma Z, et al. A mixed samples-driven methodology based on denoising diffusion probabilistic model for identifying damage in carbon fiber composite structures. IEEE Trans Instrum Meas. 2023;72:1-11. doi: 10.1109/TIM.2023.3267522
- [25] Kim JW, Park S. Magnetic flux leakage sensing and artificial neural network pattern recognition-based automated damage detection and quantification for wire rope non-destructive evaluation. Sensors. 2018;18(1):109. doi: 10.3390/s18010109



- [26] Yi W, Chan WK, Lee HH, et al. An uncertainty-aware deep learning model for reliable detection of steel wire rope defects. IEEE Trans Rel. 2024;73(2):1187-1201. doi: 10.1109/TR. 2023.3335958
- [27] Liu S, Chen M. Wire rope defect recognition method based on mfl signal analysis and 1d-cnns. Sensors. 2023;23(7):3366. doi: 10.3390/s23073366
- [28] Liu S, Liu Y, Shan L, et al. Hybrid conditional kernel sym for wire rope defect recognition. IEEE Trans Ind Inf. 2024;20(4):6234–6244. doi: 10.1109/TII.2023.3344135
- [29] Zhang Y, Feng Z, Shi S, et al. A quantitative identification method based on cwt and cnn for external and inner broken wires of steel wire ropes. Heliyon. 2022;8(11):e11623. doi: 10. 1016/j.heliyon.2022.e11623
- [30] Liu S, Hua X, Liu Y, et al. Accurate wire rope defect mfl detection using improved Hilbert transform and lstm neural network. Nondestr Test Eval. 2024;40(4):1379-1408. doi: 10. 1080/10589759.2024.2351141
- [31] Zhao M, Zhang D, Zhou Z. The research on quantitative inspection technology to wire rope defect based on hall sensor array. Nondestr Test. 2012;34:57-60.
- [32] Tan X, Zhang J. Evaluation of composite wire ropes using unsaturated magnetic excitation and reconstruction image with super-resolution. Appl Sci. 2018;8(5):767. doi: 10.3390/ app8050767
- [33] Zheng P, Zhang J. Quantitative nondestructive testing of wire rope based on pseudo-color image enhancement technology. Nondestr Test Eval. 2019;34(3):221-242. doi: 10.1080/ 10589759.2019.1590827
- [34] Zhou Z, Liu Z. Fault diagnosis of steel wire ropes based on magnetic flux leakage imaging under strong shaking and strand noises. IEEE Trans Ind Electron. 2021;68(3):2543-2553. doi: 10.1109/TIE.2020.2973874
- [35] Liu Z, Ren L. Shaking noise exploration and elimination for detecting local flaws of steel wire ropes based on magnetic flux leakages. IEEE Trans Ind Electron. 2023;70 (4):4206-4216. doi: 10.1109/TIE.2022.3174302
- [36] Pan F, Liu Z, Ren L, et al. Adaptive local flaw detection based on magnetic flux leakage images with a noise distortion effect for steel wire ropes. IEEE Trans Ind Electron. 2024;71 (4):4120-4129. doi: 10.1109/TIE.2023.3273250
- [37] Ren L, Liu Z, Wang H, et al. Eliminating shaking noise for defect detection of steel wire ropes based on magnetic flux leakage signals. In: 2019 IEEE 4th Advanced Information Technology, Electronic and Automation Control Conference (IAEAC), Chengdu, China: IEEE; 2019. Vol. 1. p. 1037–1041. doi: 10.1109/IAEAC47372.2019.8997698.
- [38] Yang L, Liu Z, Ren L, Liao F, and Zuo M. Quantitative detection of local flaw under the lift-off effect for steel wire ropes. IEEE Sensors J. 2024;24(16):26081–26090. doi: 10.1109/ JSEN.2024.3421650